Modeling of a semisubmersible floating wind platform in severe waves

Rivera-Arreba, I.; Bruinsma, N.; Bachynski, E. E.; Viré, A.; Paulsen, B. T.; Jacobsen, N. G.

DOI
10.1115/OMAE2018-77680

Publication date
2018

Document Version
Final published version

Published in
Offshore Geotechnics; Honoring Symposium for Professor Bernard Molin on Marine and Offshore Hydrodynamics

Citation (APA)
Rivera-Arreba, I., Bruinsma, N., Bachynski, E. E., Viré, A., Paulsen, B. T., & Jacobsen, N. G. (2018). Modeling of a semisubmersible floating wind platform in severe waves. In *Offshore Geotechnics; Honoring Symposium for Professor Bernard Molin on Marine and Offshore Hydrodynamics* (Vol. 9). Article OMAE2018-77680 ASME. https://doi.org/10.1115/OMAE2018-77680

MODELING OF A SEMISUBMERSIBLE FLOATING WIND PLATFORM IN SEVERE WAVES

Irene Rivera-Arreba*
Delft University of Technology
Delft, The Netherlands
Email: i.riveraarreba@tudelft.nl

Niek Bruinsma
Deltares
Delft, The Netherlands
Email: niek.bruinsma@deltares.nl

Erin E. Bachynski
Norwegian University of Science and Technology
Trondheim, Norway
Email: erin.bachynski@ntnu.no

Axelle Viré
Delft University of Technology
Delft, The Netherlands
Email: axelle.vire@tudelft.nl

Bo T. Paulsen
Deltares
Delft, The Netherlands
Email: @deltares.nl

Niels G. Jacobsen
Deltares
Delft, The Netherlands
Email: niels.jacobsen@deltares.nl

Floating offshore wind platforms may be subjected to severe sea states, which include both steep and long waves. The hydrodynamic models used in the offshore industry are typically based on potential-flow theory and/or Morison's equation. These methods are computationally efficient, and can be applied in global dynamic analysis considering wind loads and mooring system dynamics. However, they may not capture important nonlinearities in extreme situations. The present work compares a fully nonlinear wave tank (NWT), based on the viscous Navier-Stokes equations, and a second-order potential-flow model for such situations.

A validation of the NWT is first completed for a moored vertical floating cylinder. The OC5-semisubmersible floating platform is then modelled numerically both in this nonlinear NWT and using a second-order potential-flow based solver. To validate both models, they are subjected to non-steep waves and the response in heave and pitch is compared to experimental data.

More extreme conditions are examined with both models. Their comparison shows that if the structure is excited at its heave natural frequency, the dependence of the response in heave on the wave height and the viscous effects cannot be captured by the adjusted potential-flow based model. However, closer to the inertia-dominated region, the two models yield similar responses in pitch and heave.

*Address all correspondence to this author.

1 INTRODUCTION

Floating wind turbines (FWTs) are proposed as a method to harness the significant wind energy resource in deep water. International research efforts have led to the development of coupled numerical global analysis tools for FWTs in order to understand their behaviour under wind and wave actions. Examples of these are the series of projects that the International Energy Agency (IEA) has facilitated in order to improve offshore wind modelling tools. The *Offshore Code Comparison Collaboration* project (OC3, [1]), its Continuation (OC4, [2]), and with Correlation (OC5, [3]), aim to verify and validate the accuracy of complex engineering tools through code-to-code and code-to-data comparisons. The latest one deals with the dynamic analysis of the DeepCWind semisubmersible floating wind platform [4], on which the 5MW-NREL wind turbine is mounted [5]. The hydrodynamic models in such tools are usually based on first- (and second-) order potential-flow theory, sometimes also including Morison's equation.

To model highly nonlinear waves, understand their interaction with a floating platform, and obtain estimates of the resulting loads on the structure, other approaches that account for higher-order phenomena are generally needed. For instance, Bachynski and Moan [6] studied the third-order high-frequency loads on a Tension Leg Platform (TLP) wind turbine. Here the potential-flow based Faltinsen-Newman-Vinje (FNV) formula (Faltinsen et al. [7]) was used. Chan et al. [8] applied the fluid-impulse theory (FIT) to calculate the nonlinear surge diffraction force on the MIT/NREL TLP turbine. This theory allows the evaluation of second- and

higher-order nonlinear effects using compact force expressions, applied as time derivatives of impulses. Whereas the named approaches are based on potential-flow theory, computational fluid dynamics (CFD) account for the fully nonlinear terms of the Navier-Stokes equations. CFD was used by Benitz et al. (2014) [9] to evaluate the wave loads on the OC4-semisubmersible. At a later stage, in [10], the geometry factors to be considered when defining drag coefficients at the heave plates of the OC5-semisubmersible were studied. The findings were applied to a less computationally expensive potential-flow based tool.

In the current study, two different numerical approaches were applied: a fully nonlinear Navier-Stokes/VOF solver (referred to as Navier-Stokes model from here on) and a second-order potential-flow theory solver (referred to as potential-flow model). The fully nonlinear Navier-Stokes/VOF numerical wave tank was developed within the open-source CFD toolbox OpenFOAM® framework (version 1606+) [11]. To model the motions of the floating structure, together with the generation and absorption of the waves, the interDyMFoam solver was extended with the waves2Foam package (Jacobsen et al. [12]). Additionally, the potential-flow model of the OC5-semisubmersible floating platform was generated with the DNV-GL software tools Wadam and SIMO-RIFLEX. Once both models were validated, they were compared in order to assess the performance of the potential-flow model in two different conditions where nonlinearities are of relevance.

Sections 2 and 3 describe the two numerical models used throughout the current work, respectively. The validation of the nonlinear numerical wave tank for a floating cylinder is detailed in Section 4, whereas the validation of both numerical models of the OC5-semisubmersible platform, and their comparison and performance are detailed in Section 5. The conclusions are presented in Section 6.

2 NAVIER-STOKES MODEL

The governing equations for an incompressible Newtonian fluid are based on the continuity and the momentum conservation laws, which expressed in their differential form, yield:

$$\nabla \cdot \mathbf{u} = 0; \tag{1}$$

$$\frac{\partial \rho \mathbf{u}}{\partial t} + \nabla \cdot \rho \mathbf{u}\mathbf{u}^T = -\nabla p^* + (\mathbf{g}\cdot\mathbf{x})\nabla\rho + \nabla \cdot \mu_{tot}\nabla\mathbf{u}, \tag{2}$$

where $\nabla = (\partial_x, \partial_y, \partial_z)$ is the three-dimensional gradient operator, $\mathbf{u}$ the velocity field in Cartesian coordinates, $\mathbf{g}$ the vector of acceleration due to gravity, $\mathbf{x} = (x, y, z)$ the Cartesian coordinate vector and p^* the excess pressure, equal to $p^* = p - \rho(\mathbf{g}\cdot\mathbf{x})$, where p is the total pressure. The local density ρ and the total dynamic viscosity μ_{tot}, defined in terms of the water and air volume fraction α (subscripts a and w, respectively), with $\phi = \rho, \mu_{tot}$ are formulated as:

$$\phi = \alpha\phi_w + \phi_a(1-\alpha). \tag{3}$$

To solve these equations, OpenFOAM® uses the volume of fluid (VOF) method, developed by Hirt & Nichols [13], in which the scalar function $\alpha \in [0,1]$ represents the phase of the fluid in each cell (0 is air, 1 is water). This field is advanced in time once the velocity is known, following the modified transport equation, formulated by Rusche [14]:

$$\frac{\partial \alpha}{\partial t} + \nabla \cdot \mathbf{u}\alpha + \nabla \cdot \mathbf{u}_r\alpha(1-\alpha) = 0. \tag{4}$$

The additional convective term keeps the interface sharp, even with the step-like nature of α. $\mathbf{u}_r$ is an artificial velocity field suitable to compress the interface. It exists if $0 < \alpha < 1$, i.e. in the vicinity of the interface, and its magnitude is proportional to the instantaneous velocity, see e.g. Berberović et al. (2009) [15] for details. To ensure boundedness of the solution, a multidimensional flux limited scheme, namely the Multidimensional Universal Limited for Explicit Solution (MULES), was used.

2.1 Boundary conditions

To solve the integral form of the incompressible Navier-Stokes equations at every point of the numerical domain, boundary conditions were imposed on all the surfaces.

The velocity and the α field boundary conditions at the inlet and outlet surfaces were given by the applied wave theory. At the seabed, a *slip* condition was imposed, which directly implies that the viscous boundary layer effects, such as the shear stresses, were neglected. At the front and back walls a *slip* condition was applied. At the upper wall boundary, the total pressure was set equal to zero, and an *atmospheric* boundary condition was set for α and the velocity. This means that air and water are allowed to leave the numerical domain, while only air is allowed to flow back in. The total pressure at the atmosphere boundary is equal to zero. At the surface of the body a *no slip* condition was applied. This implies that the effect of viscosity and turbulence generation is not neglected at the walls, and phenomena such as wave breaking or splashing near the structure are included. However, the viscous boundary layer is not resolved, since the grid is not fine enough, and no turbulence models were implemented in this work. Their use may influence the propagation of the free surface (see Brown et al. [16]), so the research on more appropriate models for these applications is still on-going. A schematic view of the domain, including the relaxation zones, is depicted in Fig. 1.

2.2 Relaxation zones

The open-source wave generation and absorption toolbox *waves2Foam* utilises relaxation zones, to avoid reflections from the boundaries. The relaxation zones can have an arbitrary shape, although for the cases treated here the shape was always rectangular in the horizontal plane. The relaxation zone at the inlet is used to generate the incoming waves. Since the exact hydrodynamic conditions in the experimental cases are not exactly known, its reproduction is usually not possible. Therefore the fully nonlinear stream function

theory (see Fenton [17]), was applied for every regular wave case. The relaxation zone at the outlet was set as a still current with no velocity.

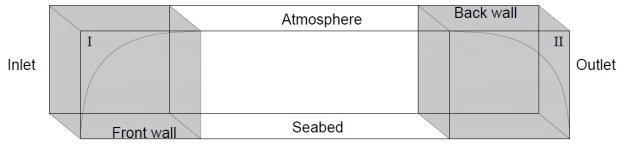

Fig. 1. Schematic overview of the boundary conditions implemented at the computational domain in the Navier-Stokes solver, where I and II correspond to the relaxation zones.

2.3 Domain discretisation

OpenFOAM® uses the finite volume (FV) method of discretisation, based on the application of the conservation principles applied to a finite region in space known as control-volume. Here the spatial discretisation is based on the number of points per cylinder diameter (p.p.c.d.) or per wavelength (p.p.w.l.), measured at the free surface. For the background domain discretisation the utility *blockMesh* was used, whereas for the refinement of the mesh around the body, *snappyHexMesh* was applied. For the temporal discretisation the Courant-Friedrichs-Lewy (CFL) condition, with a maximum Courant number of 0.25, was used.

2.4 Temporal and spatial discretisation schemes

Differential schemes are implemented for the numerical approximation of the terms in the governing equations. The treatment of the advective term of the Navier-Stokes equation (Eq. 2) is done based on the conclusions presented by Bruinsma et al. [18]. Here a first-order upwind and a second-order MUSCL scheme (TVD) were compared, and the former was used throughout the current numerical analysis. An overview of the discretisation schemes applied throughout this work is given in Tab. 1.

Stability of the numerical model can be ensured by two different pressure-velocity coupling stability methods: the *under-relaxation* or the *predictor-corrector* method. The *under-relaxation* method applies a relaxation factor f_a to the computed acceleration from the forces and moments, as:

$$a_i^* = f_a a_i + (1 - f_a) a_{i-1}^*, \tag{5}$$

where a_i^* is the under-relaxed acceleration of the center of gravity (*COG*) at the instantaneous time step. In this case, the acceleration is treated as a total variation diminishing (TVD) property. This avoids high frequency oscillations from the time integration, by applying a monotonicity criterion. Although it increases the stability, a diffusive term is introduced, which may affect the convergence rate of the solution. The *predictor-corrector method* implies an initial step of predicting the displacement of the body based on the forces acting on it. During the correcting steps the pressure field is updated and the corrected displacement of the body is applied. To achieve a smooth convergence, the pressure is relaxed with the relaxation factor f_p, as:

$$p_i^* = f_p p_i + (1 - f_p) p_{i-1}^*, \tag{6}$$

where p_i^* is the under-relaxed pressure at the instantaneous time step. In this work, a constant under-relaxation factor f_p, equal to 0.5, was applied during all the iteration loops, except for the last one, in which f_p was set to 1.0, to ensure time consistency.

Table 1. Numerical schemes used.

Term	Discretisation
Spatial domain	FV method.
Temporal derivative: $\frac{d}{dt}$	Euler. First-order.
Gradient: $(\nabla \mathbf{u}, \nabla \alpha)$	Gauss linear.
Divergence: $\nabla \cdot (\rho \phi \mathbf{u})$	Gauss upwind.
$\nabla \cdot (\phi \alpha)$	Gauss upwind.
$\nabla \cdot (\rho \phi_{rb} \alpha)$	Gauss interface compression.
Laplacian: ∇^2	Gauss linear corrected.

3 SECOND-ORDER POTENTIAL-FLOW THEORY MODEL

Potential-flow solvers, also known as diffraction solvers, predict wave-induced motions and loads on large volume structures at zero velocity. The main assumption of potential-flow theory is that the fluid is inviscid and incompressible. The velocity field $\mathbf{u}$ can thus be defined by the velocity potential $\phi(\mathbf{x},t)$ as:

$$\mathbf{u} = \nabla \phi = \left(\frac{\partial \phi}{\partial x}, \frac{\partial \phi}{\partial y}, \frac{\partial \phi}{\partial z} \right). \tag{7}$$

If the continuity equation for incompressible flows is invoked, the velocity potential has to satisfy Laplace's Equation (Eq. 8) in the fluid domain, as:

$$\nabla^2 \phi(\mathbf{x},t) = 0. \tag{8}$$

The number of unknowns is reduced from four, namely the three velocity components and the pressure, to just the scalar velocity potential ϕ. The pressure p is then computed by the unsteady Bernoulli's equation. Together with the boundary conditions, the Boundary Value Problem (BVP) is defined, and solved by one of the most widespread methods: the Boundary Element Method (BEM), also known as panel method [19]. The boundary conditions include all the terms up to the second-order, based on a perturbation approach, see [20]. The equation of motion of a rigid floating body with six degrees of freedom in a regular wave in the frequency-domain ω is given by:

$$\overline{X}(\omega) \left[-\omega^2 \left(\overline{\overline{M}} + \overline{\overline{A}}(\omega) \right) + i\omega \overline{\overline{B}}(\omega) + \overline{\overline{C}} \right] = \overline{F_{exc}}(\omega), \tag{9}$$

where $\overline{\overline{M}}$ is the inertia matrix, $\overline{\overline{A}}$ the added mass force matrix, $\overline{\overline{B}}$ the potential damping force matrix, $\overline{\overline{C}}$ the stiffness matrix and $\overline{F_{exc}}$ the excitation force vector. In this work, the frequency-dependent elements were solved with Wadam [21], which evaluates the unsteady hydrodynamic pressure on the body, loads and motions of the body, as well as the induced pressure and velocity in the fluid domain. The Gauss direct-solver was used and the irregular frequencies that lead to numerical inaccuracies were removed [20].

To carry out the time-domain simulations RIFLEX-SIMO, developed by SINTEF Ocean, was used. Here, the frequency-dependent hydrodynamic properties are transformed by means of a retardation function $\overline{\overline{k}}(t)$, based on the convolution theory. Expressed in terms of the infinite-frequency limit added mass $\overline{\overline{A_\infty}}$, and the retardation function, Eq. (9) in the time-domain reads:

$$\left(\overline{\overline{M}}+\overline{\overline{A_\infty}}\right)\ddot{\bar{x}}(t)+\int_0^t \overline{\overline{k}}(t-\tau)\,\dot{\bar{x}}(\tau)d\tau+\overline{\overline{C}}\,\bar{x}(t)=\overline{f_{exc}}(t). \quad (10)$$

The time convolution of the radiation impulse-response functions with the platform velocities allows accounting for the linear memory effects within the time-domain hydrodynamic model. The time-domain integration in the current case was done using the third-order accurate Runge-Kutta numerical method.

For cylindrical structures with small diameters, viscous forces and flow separation have to be taken into account when severe sea states with long waves and high wave heights take place. In these cases, the potential-flow solution for large volume bodies is combined with Morison's equation [22], which includes a drag term in addition to the inertial forces one.

Relevant second-order hydrodynamics effects were modelled, which include the difference-frequency quadratic transfer function and mean drift forces. The latter are based on Newman approximation [23], which depends on first order computations.

4 CASE-STUDY 1: VALIDATION OF THE NAVIER-STOKES MODEL

The validation of the Navier-Stokes numerical model for a floating cylinder, based on the 6DOF (degree of freedom) solver *waveDyMFoam*, was done according to the experimental data from Palm et al. [24]. The structural properties of the cylinder are the same as in the experimental model, see Table 2. The dimensions of the numerical domain are shorter than the ones of the physical model. However, these were ensured to be long enough to avoid any reflections. The numerical set-up is the same for all the cases that are presented here, i.e. for the decay tests and the cylinder subjected to waves. These are indicated in Figure 2.

4.1 Decay tests in heave and pitch

The responses in heave and pitch, normalised by the respective initial displacements, are depicted in Figure 3. In order

Table 2. Floating cylinder structural properties.

d [m]	Draft [m]	Mass [kg]	KG [m]	I_{xx} [kgm^2]
0.515	0.172	35.85	0.0758	0.9

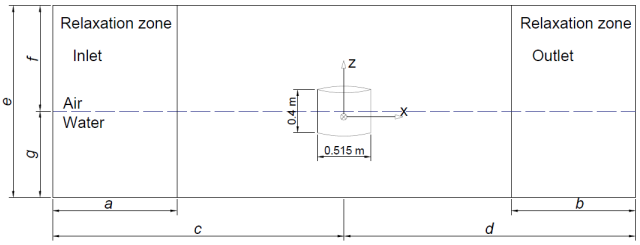

Fig. 2. Numerical domain set-up, with the dimensions indicated with letters in meters, cylinder diameters (D) and wave lengths (w.l.): a = 3 m = 5.80 D; b = 6 m = 11.65 D = c; d = 9 m = 17.50 D; e = 1.8 m; f = g = 0.9 m. The width of the domain is 5 m.

to ensure convergence in heave, three different background mesh lengths were used: 10, 15 and 20 points per cylinder diameter (p.p.c.d.). Whereas the background mesh was contant along the numerical wave tank, a refinement around the cylinder was applied. The coarsest mesh presents a large difference in damping, and also in natural period, with an error six times larger than the finest grid. The difference in period of the latter with respect to the experiments is 0.08%.

Due to the low difference between the 15 and 20 p.p.c.d. meshes, the former was used for the pitch decay test. In this case, for the structural properties as indicated in the work of Palm et al. (see Table) the damping is properly captured, but the difference in period is of more than 6% with respect to the experimental data. The reason may be found in the structural properties of the cylinder. A sensitivity analysis on those is depicted in Figure 3, bottom. For an inertia of 0.95 kgm^2 and a KG of 0.0818 m the error decreases to 1.7%.

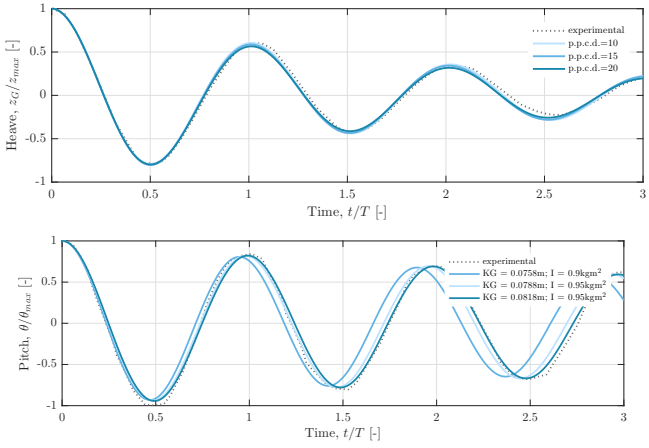

Fig. 3. Decay tests in heave (top) and pitch (bottom). The displacements are normalised by the maximum initial values, 0.076 m and 8.88°, repectively, and the time by the experimental natural periods, which are 1.11 s in heave and 1.17 s in pitch.

The natural periods in heave and pitch are close to each other, which yields a cross-coupling between these modes. The exchange of energy between these is depicted in Figure 4, which corresponds to the response in heave and pitch for the pitch decay test. Please note that the response is not normalised in this case. Whereas the pitch response dampens out, the response in heave increases.
The pitch motion, decoupled from surge, is described as:

$$(I_{55}+A_{55})\frac{d^2x_5}{dt^2}+B_{55}\frac{dx_5}{dt}+C_{55}(t)x_5=0, \qquad (11)$$

with C_{55} equal to $\rho g V\,(GM_{Tm}+\delta GM_T\sin(\omega_e t))$, where δGM_{Tm}, ω_e and β are, respectively, the amplitude of the time oscillations of the transverse metacentric height GM_T, its frequency and its phase. These oscillations are caused in the current case by the heave and pitch motions. GM_{Tm} is the mean transverse metacentric height, associated with the mean restoring coefficient in pitch. If Equation 11 is divided by $(I_{55}+A_{55})$, it yields:

$$\frac{d^2x_5}{dt^2}+2\xi\omega_n\frac{dx_5}{dt}+\omega_n^2\left[1+\frac{\delta GM_T}{GM_{Tm}}\sin(\omega_e t)\right]x_5=0, \qquad (12)$$

where $\xi=B_{55}/[2(I_{55}+A_{55})\omega_n]$ is the fraction of the damping relative to the critical one and $\omega_n=2\pi\sqrt{\dfrac{C_{55}}{(I_{55}+A_{55})}}$. Equation 12 is known as Mathieu's (damped) equation, which is a specific case of the second-order ODE Hill's equation. The condition of instability may be identified using a parametric plane, shown in Figure 4 (bottom), also known as *Strutt diagram*. Its derivation is based on the solution of the Hill's equation with the Mathieu parameters α and $\delta GM_T/GM_{Tm}$ [25]. In the current case, α and $\delta GM_T/GM_{Tm}$ are approximately equal to unity (green point in the figure). The damping of the system, as well as the increment of α, reduce the area of instability. However, in this case, the damping ξ is calculated and proven to not be high enough to avoid the region of instability.

The identification of this instability arising confirms that the numerical model is able capture these type of instabilities, arising from nonlinearities. This, together with the low error when reproducing the decay tests in period and damping, serves as the first validation of the numerical wave tank.

4.2 Wave-structure interaction

The second validation concerning the vertical floating cylinder was done based on the response of the body to incoming regular waves. These were generated at the inlet (see Fig. 1) as a stream function, with the parameters indicated in Tab. 3. Prior to placing the body in the numerical wave tank, the surface elevation computed with *waveFoam* was compared to the stream function analytical solution, as presented in

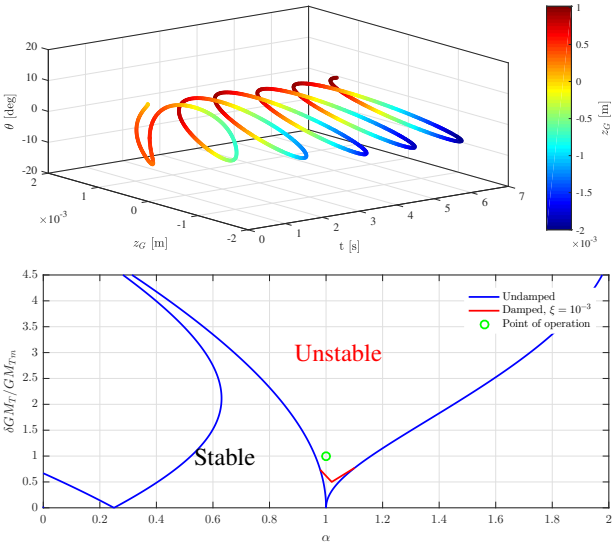

Fig. 4. Top: heave response for the pitch decay test. Bottom: stability diagram for the undamped Mathieu's equation.

Fig. 6. A multi-grading meshing technique was applied to these cases, to be as efficient as possible. The number of cells per wave height in the z-direction at the free-surface region is 400. This number decreases linearly in the positive and negative z-direction. In the x-direction, the number of cells per wavelength is 67, or 15 p.p.c.d., upstream of where the body is placed. Downstream the number of cells decreases linearly in the positive x-direction. In the y-direction the cells are uniformly distributed. The background mesh is depicted in Figure 5. The amplitude of the first harmonic of the generated wave is in good agreement with the analytical solution of the stream function (Fig. 6), with a wave amplitude attenuation caused by numerical diffusion of less than 3% at $x/D=0$, where the *COG* of the cylinder is to be placed.

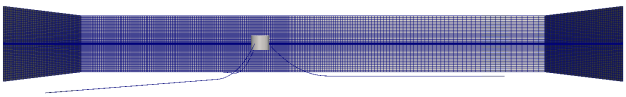

Fig. 5. Overview of the background mesh for the floating cylinder.

Table 3. Regular waves (stream function) parameters.

f [Hz]	T [s]	H [m]	λ [m]	$\dfrac{d}{gT^2}$	$\dfrac{H}{gT^2}$
0.83	1.2	0.04	2.23	0.063	0.00283

Figure 7 presents the motions of the moored cylinder as a result of the regular incoming waves for four wave periods at the end of the simulation. The previous ones were discarded to avoid the ramping-up of the wave and the initial impact on the body. The response was computed for the two

pressure-velocity coupling stability methods previously discussed. The vertical motions are in good agreement, with a crest-to-trough difference of less than 8% in heave and 9% in pitch, compared to the experimental data.

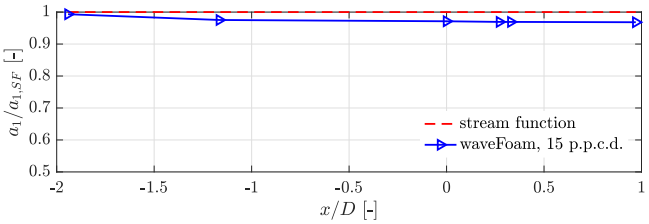

Fig. 6. First harmonic amplitude a_1, normalised by the first harmonic amplitude of the analytical solution $a_{1,SF}$.

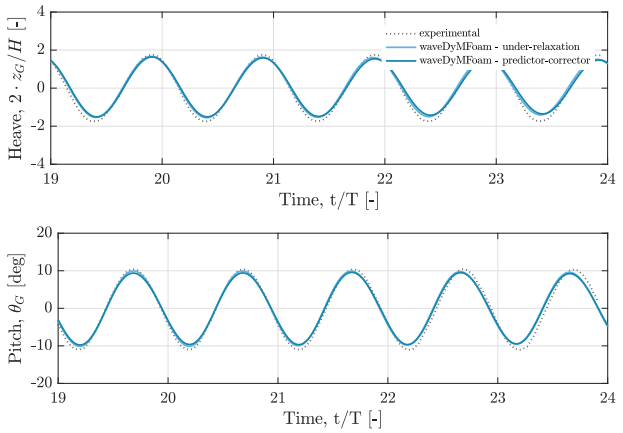

Fig. 7. Response of the floating cylinder due to an incoming regular wave in heave (top) and pitch (bottom). The heave time series is normalised by the wave height. The time is normalised by the incoming wave period.

5 CASE-STUDY 2: OC5-SEMISUBMERSIBLE FLOATING WIND PLATFORM

The Offshore Code Comparison, Collaboration, Continued, with Correlation (OC5) project is run under the IEA Wind Research Task 30 and is focused on validating the tools used for modelling offshore wind systems through the comparison of simulated responses of several designs to physical test data. As part of the *TO2 Floating Wind* research project, a series of 1:50 scale model tests were completed in the concept basin at MARIN, see [26]. Here the hydrodynamics of the moored semisubmersible platform DeepCWind (or OC5-semisubmersible) were investigated. The full-scale dimensions and structural properties of the platform are presented in [3].

To model the first- and second-order hydrodynamics in the potential-flow solver, a hybrid formulation that considers both a potential-flow solution and a viscous drag from the strip-theory (Morison's Equation) solution was applied. The

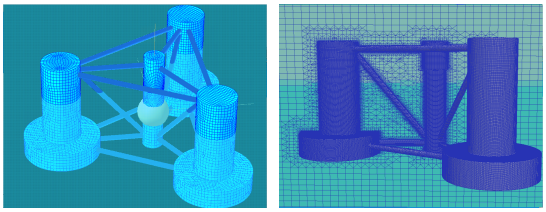

Fig. 8. OC5-semisubmersible models in the two numerical frameworks: the potential-flow model (left) and the Navier-Stokes model (right). In the potential-flow model, the main columns, the central column and the heave plates are depicted in light blue.

former was used for the large-volume members and the latter for the slender elements. Since the model is symmetric around the OXZ plane, just half of it was modelled and meshed uniformly with 5300 elements. Based on the values obtained from the experimental decay tests' data, the nonlinear viscous drag contribution from the main and slender members was implemented in the frequency-domain analysis. The mooring lines' effects were modelled by an additional stiffness matrix for the hydrodynamic calculations. This approach is static (and linear), as opposed to the nonlinear quasi-static one applied in the Navier-Stokes model mooring system. Figure 8 shows the OC5-semisubmersible potential-flow and Navier-Stokes models.

5.1 Heave and pitch moored decay tests

To validate the potential-flow model, moored decay tests were computed and compared against the experimental data and the Navier-Stokes model. Note that all the values are presented in full-scale, unless otherwise specified. For the heave decay test an initial displacement of 1 m was applied. The response is presented in Fig. 9 (top). The natural period is well captured by both numerical models (Tab. 4). However, the damping is larger after $t/T = 2$. The linear-plus-quadratic damping coefficients b_1 and b_2 are obtained based on establishing the loss of energy slope at each cycle, see [27]. The coefficients are shown in Tab. 5 for the experimental and the potential-flow models. Despite the difference in damping, the numerical models show good correspondence.

The pitch unforced response (Fig. 9, bottom) of the potential-flow model, with an initial rotation angle of 3.34°, is in agreement with the Navier-Stokes model. The quadratic damping is better captured, whereas the overall damping seems to be better reproduced after $t/T = 1$. Even though the natural period of the numerical solutions is shorter, the difference is a mere 1%. It can thus be concluded that both the numerical models are able to reproduce the behaviour of the floating platform.

Table 4. First natural periods in heave and pitch for the experimental (subscript e), Navier-Stokes (NS) and potential-flow (pf) models.

DOF	T_e [s]	T_{NS} [s]	T_{pf} [s]
Heave	17.5	17.5	17.5
Pitch	33.1	33.0	32.8

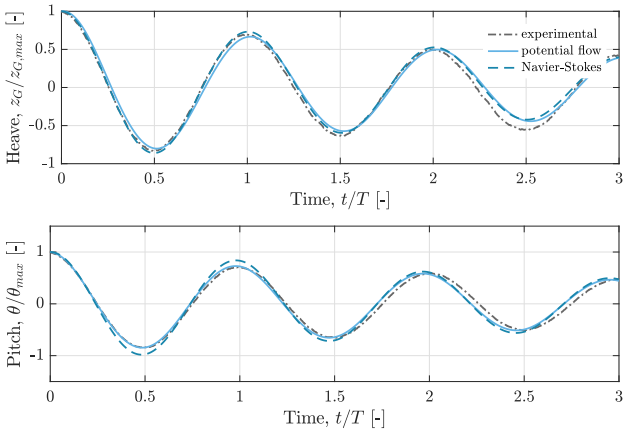

Fig. 9. Moored decay tests in heave (top) and pitch (bottom). The displacements are normalised by the maximum initial values, and the time by the experimental natural periods, which are 17.50 s for heave and 33.1 s for pitch.

Table 5. Damping coefficients calculated based on the results up to $t/T = 17$ for heave and $t/T = 10$ for pitch.

DOF	$b_{1,e}$ [m^{-1}]	$b_{1,pf}$ [s^{-1}]	$b_{2,e}$ [rad^{-1}]	$b_{2,pf}$ [s^{-1}]
Heave	0.0055	0.0063	0.074	0.126
Pitch	0.0039	0.0049	0.025	0.028

5.2 Wave-structure interaction

Besides the validation of the numerical models based on decay tests, the structure was subjected to a regular incoming wave whose characteristics are presented in Tab. 6. The dimensions of the computational domain for the Navier-Stokes model are indicated in Fig. 10.

Table 6. Regular wave (stream function) parameters.

f [Hz]	T [s]	H [m]	λ [m]	$\frac{d}{gT^2}$	$\frac{H}{gT^2}$
0.08	12.1	7.1	231.0	0.139	0.005

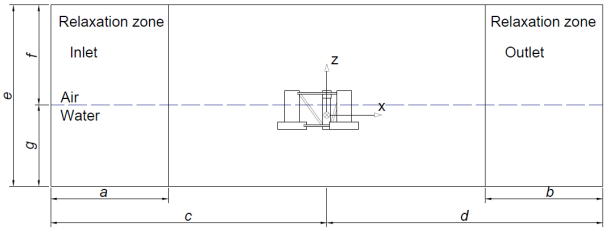

Fig. 10. Overview of the OC5-semisubmersible numerical set-up, without moorings, for the wave-structure validation cases against the experimental data. The dimensions, in model-scale, are denoted with letters, which correspond to: a = b = 4.65 m = 1.6 w.l.; c = d = 6.5 m; e = 5.2 m; f = 1.2 m; g = 4 m. The width of the domain is 4 m.

A mesh convergence study for both the undisturbed surface elevation and the structure response in heave and pitch is presented in Fig. 11. The free surface elevation was measured at the same x-coordinate where the *COG* of the body was placed. It is seen that the solution of the Navier-Stokes model converges, with a difference between the highest and the lowest grid refinements in average crest-to-trough amplitude of less than 2% in heave and 5% in pitch. Consequently, a mesh refinement of 50 p.p.w.l. was used for the successive cases, unless otherwise specified.

Figure 12 presents the time series of the wave elevation for the potential-flow and the Navier-Stokes models, together with the response of the moored structure in heave and pitch, for the finest grid. The surface elevation is in good agreement. A higher crest and smoother trough are observed in the Navier-Stokes model, since the wave cannot be described as fully linear anymore. From $t/T = 6$, the amplitude complies with the experimental data for both numerical models. The ramping-up process is depicted in the experimental data time series and the Navier-Stokes model response. The potential-flow model response in heave matches both the experimental and the nonlinear Navier-Stokes model. A lower frequency component is identified in the latter at 0.028 Hz, which indicates that the pitch is excited around its first natural frequency by the third harmonic of the wave. Due to the crossed-coupling between modes, it shows up in the heave

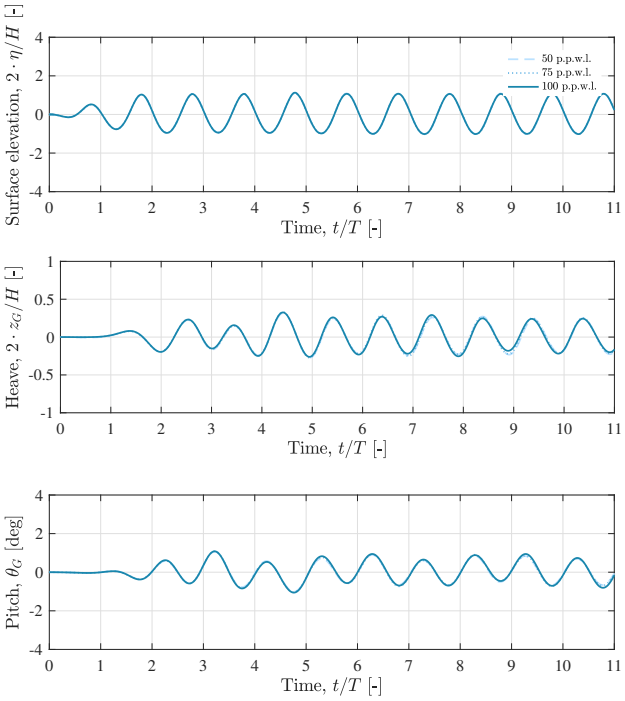

Fig. 11. Mesh convergence study for the free surface elevation (top), heave (mid) and pitch (bottom) responses of the moored OC5-semisubmersible to an incoming regular wave of 12.1 s period.

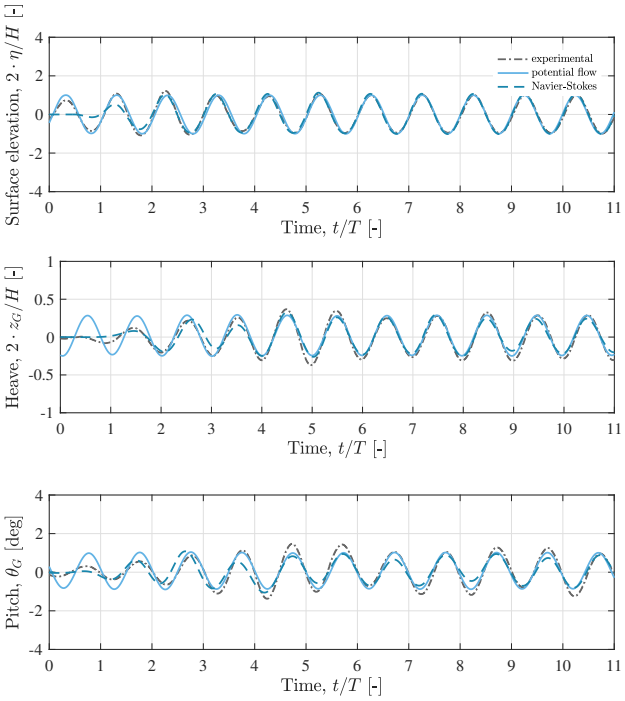

Fig. 12. Comparison of the free surface elevation (top), heave (mid) and pitch (bottom) response of the moored floating platform with the experimental data to an incoming regular wave of 12.1 s period.

motion. Both responses present an almost negligible phase shift in heave with respect to the wave elevation. For the pitch response, a good agreement with the experimental data is observed. Both the experimental and the Navier-Stokes models show again a lower frequency component, around the pitch natural frequency.

5.3 Response in heave resonance conditions

The natural periods of the semisubmersible floating platform treated here in pitch and roll are over 30 s. At these periods the wave energy is expected to be small, and therefore large resonant motions are not likely to take place in these modes. However, the heave natural period is lower than 20 s, which can be excited by waves with similar periods, especially swell waves. The response under swell conditions was studied by subjecting the semisubmersible to the regular incoming wave defined in Tab. 7. To estimate the length of the domain given such a large wave length, a propagation study of the wave without the presence of the structure in the numerical wave tank was done, to verify that no reflections from the boundaries occurred. After several iterations, the minimum length of the numerical domain required to avoid any disturbances is 22 m (in model scale), with the absorption zone of at least one wave length long. The dimensions of the numerical wave tank for this case are: a = 0.2 w.l., b = 1.1 w.l., c = 0.3 w.l. and d = 2.0 w.l., where the letters are shown in Fig. 10. Dimensions e, f and g, as well as the width, did not change. The same multi-grading meshing strategy as for the floating vertical cylinder was followed: in the positive x-direction, from the wave generation zone up to one diameter length downstream the body, the cells have constant aspect ratio equal to unity, which yielded 100 p.p.w.l. This leads to a wave amplitude attenuation, caused by numerical diffusion, of less than 4% at the point where the structure was to be placed. Downstream the body, the number of points decreases linearly in the positive x-direction. The response of the structure to the 17.4 s wave period is presented in Fig. 13. The undisturbed free surface elevation at the generation zone, as well as its phase, is in complete agreement for the two models.

Table 7. Regular wave (stream function) parameters.

f [Hz]	T [s]	H [m]	λ [m]	$\frac{d}{gT^2}$	$\frac{H}{gT^2}$
0.06	17.4	3.0	472.70	0.0673	0.001

Due to the small potential damping at this excitation frequency, the resonant motion is governed by nonlinear drag forces on the platform. The amplitude of the Navier-Stokes model heave response increases up to $t/T = 6$, from where it seems to reach a steady-state. The response of the potential-flow model is 40% lower. In these conditions the vertical velocities are larger, which have an effect on the Keulegan-Carpenter and Reynolds numbers, and therefore on the drag coefficient, as shown by Sumer & Fredsøe [28]. Furthermore, the wave height affects the transfer function in heave, particularly close to resonance, as investigated by Kirk in [29] for the specific case of semisubmersibles. Therefore, the difference in amplitude between the models does not imply

that the potential-flow model is not able to capture the heave resonant response, but that the adjustment of the model in these conditions should be dependent on the relative velocities, and studied for different wave heights. Note that the heave plates' effects on the drag forces should be investigated more precisely in the Navier-Stokes model, by implementing a higher grid refinement around these, or by studying the physical effects they imply separately.

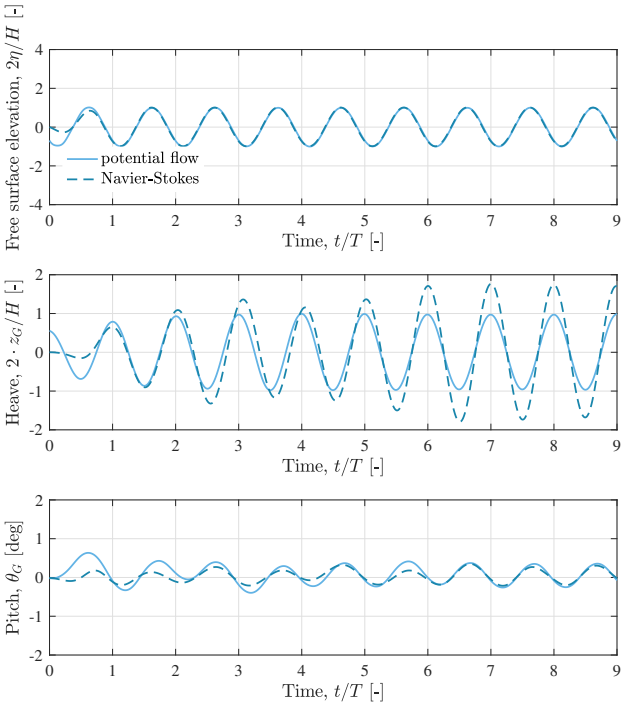

Fig. 13. Free surface elevation (top), heave (mid) and pitch (bottom) response of the moored floating platform to an incoming regular wave of 17.4 s period.

5.4 Response to waves of increasing steepness

To investigate the numerical models response to a regular wave with a steepness ratio of $H/H_{max} = 0.60$, two wave periods were considered: 8 s (0.79 rad/s) and 12.1 s (0.52 rad/s). The maximum wave height H_{max} was calculated according to Williams' [30] and Fenton's work [31]. The wave parameters for the two cases are presented in Tab. 8. The dimensions of the numerical set-up of the Navier-Stokes model are the same ones as indicated in Fig. 10.

The response in heave at 8 s excitation period is inertia dominated, which implies that the viscous forces are not as relevant. On the contrary, the second one lies in a region where the viscous forces play a relatively important role. This is illustrated in Fig. 14, where the Response Amplitude Operator (RAO) obtained from experimental data and from the potential-flow model is depicted. The latter is computed from the frequency-domain model, in which the contribution of all the elements to viscous effects is included. However, the heave plates explicit effect is included at a later stage in the time-domain simulation. Therefore the difference between the two models in the heave RAO at the so-called cancellation frequency (0.42 rad/s) is due to the disregard of the explicit heave plates effect in the drag in the frequency-domain analysis.

Table 8. Regular waves (stream function) parameters.

T [s]	H/H_{max} [-]	H [m]	λ [m]	kA [-]
12.1	0.60	25.90	249.47	0.33
8.0	0.60	8.45	108.77	0.24

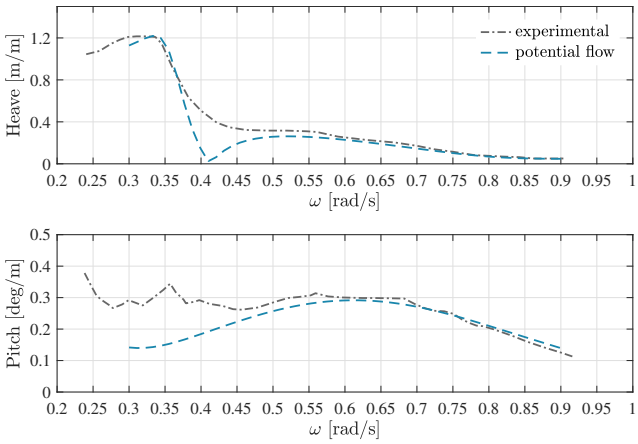

Fig. 14. Response amplitude operator in heave and pitch for the experimental and the potential-flow models.

The responses in heave and pitch for 8 s and 12.1 s wave periods and an incident wave height ratio of $H/H_{max} = 0.60$ are presented in Fig. 15. The free surface elevation shows the same difference between the models for both cases. It presents a higher crest and a smoother trough in the Navier-Stokes model, since the wave is not linear anymore.

Regarding the vertical motions, both models show a transient response up to $t/T = 6$, from where steady-state is reached. In the first case the motions are lower compared to the incoming wave height, which complies with the RAO. The nonlinearity of the wave is identified in the response in heave of the Navier-Stokes model. The smoother trough yields a lower amplitude of the motion, compared to the potential-flow model. The mean difference between the two models in crest-to-trough amplitude $|\bar{x}_i|$, calculated based on the last ten periods, is presented in Tab. 9. In the pitch time series of the Navier-Stokes model a low-frequency component is observed. It corresponds to the natural frequency in this same mode, which may be excited by the fourth harmonic of the wave.

In the second case, the response in heave is lower for the Navier-Stokes model. The reasons behind are, firstly, the shape of the nonlinear wave, and, secondly, the viscous effects. The latter were modelled based on lower relative velocities than the ones that take place in the current case.

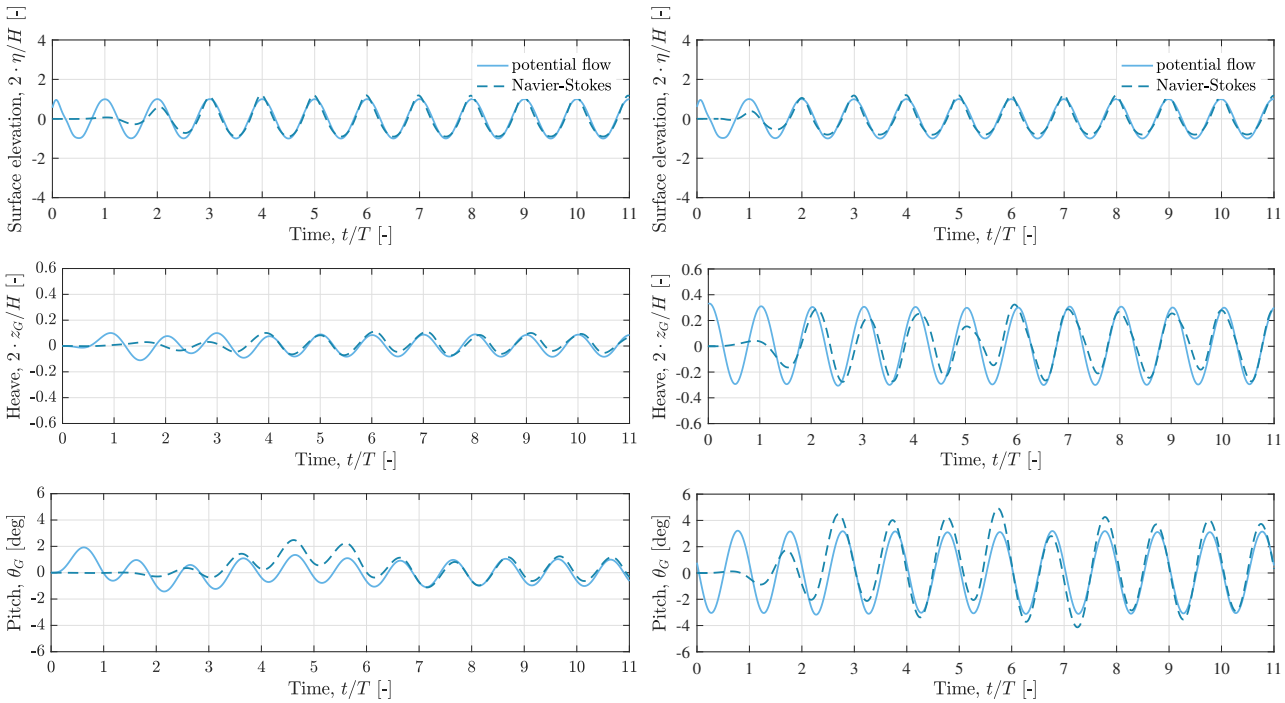

Fig. 15. Free surface elevation (top), heave (mid) and pitch (bottom) response of the moored floating platform for 8 s (left) and 12.1 s (right) regular waves period.

Since the damping is higher, the motion in the Navier-Stokes model is lower. The pitch mode is excited by the third harmonic of the wave at its natural frequency (0.18 rad/s), the same way as it was observed in the wave-structure interaction validation case. This component is not captured by the potential-flow solver, and therefore the potential-flow model response presents a lower amplitude.

Table 9. Mean crest-to-trough amplitude of the motions for both models and the difference in percentage. The values in heave motion are in meters per wave height.

T_{wave}	DOF	$\lvert\bar{x}_{i,NS}\rvert$	$\lvert\bar{x}_{i,pf}\rvert$	$\Delta\lvert\bar{x}_i\rvert$ [%]
8.0 s	Heave [m/m]	0.12	0.16	25
	Pitch [deg]	1.25	1.60	22
12.1 s	Heave [m/m]	0.50	0.58	17
	Pitch [deg]	7.40	6.20	16

6 CONCLUSION

The current work studied two numerical models for evaluating the response of floating structures: a Navier-Stokes and a potential-flow model. As a first step, the fully nonlinear Navier-Stokes model was validated for a vertical moored floating cylinder subjected to regular waves. The stability of the numerical solution was ensured by two different methods: the *acceleration-relaxation* and the *predictor-corrector* methods. Both yielded stable results and in agreement with the experimental data.

At a second stage, the hydrodynamics of the OC5-semisubmersible was modelled based on the nonlinear Navier-Stokes and the potential-flow model. Both numerical responses were validated against experimental data. The decay tests in heave and pitch showed good agreement in both the natural periods and damping. Concerning the wave-structure interaction, both models were capable of reproducing the response of the structure to non-steep regular waves. However, the potential-flow model is less computationally expensive.

Lastly, the OC5-semisubmersible response was investigated for two more extreme conditions: waves with a period close to heave resonance and waves with a higher steepness. For the first case, the response in heave of the potential-flow model showed an amplitude 40% lower than the Navier-Stokes model. The main considered reason behind is related to the transfer function dependency on the wave height, which is not implemented in the potential-flow model. Moreover, the fluid-structure relative velocities under these conditions are different to the ones used to adjust the quadratic damping of the potential-flow model, i.e. with

decay tests. Therefore closer results between the models could be achieved if the following recommendations were followed. Firstly, by adjusting the drag in the potential-flow model based on the relative velocities, and secondly, by a better investigation of the heave plates effects in the Navier-Stokes model and their implementation in the potential-flow model. The response in pitch for both numerical models showed a higher level of correspondence, which was in agreement with the RAO.

For the second case, the response in heave and pitch of the OC5-semisubmersible was investigated for waves with $H/H_{max} = 0.60$, and for two periods. The response in heave for both cases was slightly lower in the Navier-Stokes model. In the case of the 8 s wave period, the difference was caused by the nonlinearity of the wave, which presented a higher crest and a smoother trough in the Navier-Stokes model. Consequently, the amplitude in heave was lower. In the case of the 12.1 s wave period this reason applied equally. Moreover, the viscous effects played a role in the response, and although they were included in the potential-flow model, the adjustment was done for different relative velocities. The response in pitch presented a difference in the same order of magnitude as in heave. Therefore even though a higher correspondence between the models could be achieved if the quadratic drag were better investigated and adjusted, both numerical models presented a good agreement.

Acknowledgements

The authors would like to thank the Dutch research institutes Deltares, ECN, MARIN, and NLR, who participated in the *TO2 Floating Wind* project, for their contribution to the research.

References

[1] Jonkman, J., 2010. Definition of the Floating System for Phase IV of OC3. Tech. rep., National Renewable Energy Laboratory (NREL), Golden, CO.

[2] Robertson, A., Jonkman, J., Masciola, M., Song, H., Goupee, A., Coulling, A., and Luan, C., 2014. Definition of the Semisubmersible Floating System for Phase II of OC4. Tech. rep., National Renewable Energy Laboratory (NREL), Golden, CO.

[3] Robertson, A., Wendt, F., Jonkman, J., and Popko, W., 2017. "OC5 Project Phase II: Validation of Global Loads of the DeepCwind Floating Semisubmersible Wind Turbine". *Energy Procedia, 14th Deep Sea Offshore Wind R&D Conference, EERA DeepWind 2017*.

[4] Koo, B., Goupee, A., Kimball, R., and Lambrakos, K., 2014. "Model Tests for a Floating Wind Turbine on Three Different Floaters". *Offshore Mechanics and Arctic Engineering,* **136**(2).

[5] Jonkman, J., 2009. Definition of a 5-MW Reference Wind Turbine for Offshore System Development. Tech. rep., National Renewable Energy Laboratory (NREL), Golden, CO.

[6] Bachynski, E., and Moan, T., 2014. "Ringing Loads on Tension Leg Platform Wind Turbines". *Ocean Engineering,* **84**, pp. 237–248.

[7] Faltinsen, O., Newman, J., and Vinje, T., 1995. "Nonlinear Wave Loads on a Slender Vertical Cylinder". *Journal of Fluid Mechanics,* **78**, pp. 179–198.

[8] Chan, G., Sclavounos, P., Jonkman, J., and Hayman, G., 2015. "Computation of Nonlinear Hydrodynamic Loads on Floating Wind Turbines using Fluid-Impulse Theory". *Proceedings of the ASME 34th International Conference on Ocean, Offshore and Arctic Engineering (OMAE2015)*.

[9] Benitz, M., Schmidt, D., Lackner, M., Stewart, G., Jonkman, J., and Robertson, A., 2014. "Comparison of Hydrodynamic Load Predictions between Reduced Order Engineering Models and Computational Fluid Dynamics for the OC4-DeepCWind Semisubmersible". *Proceedings of the ASME 33rd International Conference on Ocean, Offshore and Arctic Engineering (OMAE2014)*.

[10] Benitz, M., Schmidt, D., Lackner, M., Stewart, G., Jonkman, J., and Robertson, A., 2015. "Validation of Hydrodynamic Load Models using CFD for the OC4-DeepCWind Semisubmersible". *Proceedings of the ASME 34th International Conference on Ocean, Offshore and Arctic Engineering (OMAE2015)*.

[11] H.G. Weller, G. Tabor, H. J. C. F., 1998. "A Tensorial Approach to Computational Continuum Mechanics using Object Oriented Techniques". *Offshore Mechanics and Arctic Engineering,* **12**(6), pp. 620–631.

[12] Jacobsen, N., Fuhrman, D., and Fredsøe, J., 2012. "A Wave Generation Toolbox for the Open-source CFD library: OpenFoam®". *International Journal for Numerical Methods in Fluids,* **70**(9), pp. 1073–1088.

[13] Hirt, C., and Nichols, B., 1981. "Volume of Fluid (VOF) Method for the Dynamics of Free Boundaries". *Journal of Computational Physics,* **39**, pp. 201–225.

[14] Rusche, H., 2002. "A Numerical Method for Two-Dimensional Studies of Large Amplitude Motions of Floating Bodies in Steep Waves". PhD thesis, Imperial College of Science, Technology & Medicine.

[15] Berberović, E., Hinsberg, N. V., Jakirlić, S., Roisman, I., and Tropea, C., 2009. "Drop Impact onto a Liquid Layer of Finite thickness: Dynamics of the Cavity Evolution". *Physical Review E - Statistical, Nonlinear, and Soft Matter Physics,* **79**(3), pp. 3–25.

[16] Brown, S., Magar, V., Greaves, D., and Conley, D., 2014. "An Evaluation of RANS Turbulence Closure Models for Spilling Breakers". *Coastal Engineering Proceedings,* **1**(34).

[17] Fenton, J., 1988. "The Numerical Solution of Steady Water Wave Problems". *Computers and Geosciences,* **14**(3), pp. 357 – 368.

[18] Bruinsma, N., Paulsen, B. T., and Jacobsen, N. G., 2017. "Validation and application of a fully nonlinear numerical wave tank for simulating floating offshore wind turbines". *International Journal of Marine Energy*.

[19] Hess, J., and Smith, A., 1964. "Calculation of

Non-lifting Potential Flow about Arbitrary Three-dimensional Bodies". *Journal of Ship Research,* **8**, pp. 22 – 44.

[20] Lee, C.-H., and Newman, J. N., 1989. "First- and Second-order Wave Effects on a Submerged Spheroid". *Journal of Ship Research*.

[21] Lee, C.-H., 1995. WAMIT. Theory Manual. Tech. rep., MIT.

[22] Morison, J., Johnson, J., and Schaaf, S., 1950. "The Force Exerted by Surface Waves on Piles". *Journal of Petroleum Technology,* **2**(5), pp. 149–154.

[23] Newman, J., 1967. "The Drift Force and Moment on Ships in Waves". *Journal of Ship Research,* **11**, pp. 51–60.

[24] Palm, J., Eskilsson, C., Paredes, G. M., and Bergdahl, L., 2016. "Coupled Mooring Analysis for Floating Wave Energy Converters using CFD: Formulation and Validation". *International Journal of Marine Energy,* **16**, pp. 83 – 99.

[25] Koo, B., Kim, M., and Randall, R., 2004. "Mathieu Instability of a Spar Platform with Moorings and Risers". *Ocean Engineering,* **31**, pp. 2175–2208.

[26] Bruinsma, N., 2016. "Validation and Application of a Fully Nonlinear Numerical Wave Tank". Master's thesis, Technical University of Delft.

[27] Roberts, J., 1985. "Estimation of Nonlinear Ship Roll Damping from Free-decay Data". *Journal of Ship Research,* **29**(2), pp. 127–138.

[28] Sumer, B. M., and Fredsøe, J., 2006. *Hydrodynamics around Cylindrical Structures*. World Scientific Publishing Co. Pte. Ltd.

[29] Kirk, C., 1985. "Resonant Heave Motion of Semisubmersible Vessels". *Ocean Engineering,* **12**(2), pp. 177–184.

[30] Williams, J., 1981. "Limiting Gravity Waves in Water of Finite Depth". *PhilosophicalTransactions of the Royal Society A: Mathematical, Physical and Engineering Sciences,* **302**(1466), pp. 139–188.

[31] Fenton, J., 1990. "Nonlinear Wave Theories". *The Sea: Ocean Engineering Science,* **9**(1), pp. 3–25.